

Ultra-Stable Zn Anode Enabled by Fiber-Directed Ion Migration Using Mass-Producible Separator

Lu Yao, Chenxin Hou, Mingqiang Liu, Haibiao Chen, Qinghe Zhao, Yan Zhao, Yuetao Wang, Lele Liu, Zu-Wei Yin, Jimin Qiu, Shunning Li,* Runzhi Qin,* and Feng Pan*

Aqueous zinc-ion battery (AZB) is a promising candidate for next-generation energy storage owing to inherent safety and low cost. However, AZBs are currently plagued by Zn dendrite growth and undesirable side-reactions, leading to poor cycling stability and premature failure. To restrain the uncontrollable Zn growth, a unique separator is developed based on polyacrylonitrile/ graphene oxide (abbreviated as PG) composite nanofibers, which contain abundance of zincophilicity functional groups to regulate the migration and distribution of Zn²⁺ ions in the separator. It is demonstrated that the cyano ligands on PG not only facilitate the dehydration of solvated Zn²⁺ ions prior to deposition, but also form fast lanes to enable homogenous scattering of deposition spots. Benefiting from these features, the PG separator offers a high ionic conductivity of 7.69 mS cm⁻¹ and a transference number of 0.74 for Zn²⁺. The Zn||Zn symmetrical cells with PG separators achieve an ultra-stable cycle life over 13 000 h. Zn||Zn_{0.27}V₂O₅ full batteries with PG separators retain 71.5% of the original capacity after 2800 cycles at a high current density of 2 A g⁻¹. This study offers future research directions toward the design of multifunctional separators to overcome the limits of Zn metal anode in AZBs.

1. Introduction

Potential fire hazards, relatively high cost, and limited natural resource of lithium for lithium-ion batteries (LIBs) have stimulated desires for safer, cheaper, and more sustainable next-generation energy storage technologies.^[1] Among all candidates,

L. Yao, C. Hou, Q. Zhao, Y. Zhao, Y. Wang, L. Liu, Z.-W. Yin, J. Qiu, S. Li, R. Qin, F. Pan

School of Advanced Materials

Peking University Shenzhen Graduate School

Shenzhen 518055, P. R. China

E-mail: lisn@pku.edu.cn; bushihaoren@pku.edu.cn;

panfeng@pkusz.edu.cn

M. Liu

Electrochemical Innovation Lab

University College London

London WC1E 7JE, UK

H. Cher

Research Institute of Materials for Integrated Circuits

Shenzhen Polytechnic

Shenzhen 518055, P. R. China



The ORCID identification number(s) for the author(s) of this article can be found under https://doi.org/10.1002/adfm.202209301.

DOI: 10.1002/adfm.202209301

aqueous zinc-ion batteries (AZBs) have the advantages of inherent safety, lowcost, natural-resources abundance, and environmental-friendliness compared to LIBs.[2] In comparison to other multivalent metals, such as Mg, Ca, and Al,[3] Zn anode offers a high theoretical specific capacity (volumetric capacity of 5855 mAh cm⁻³ or gravimetric capacity of 820 mAh g⁻¹) and meanwhile a low redox potential (-0.76 V vs standard hydrogen electrode).[4] However, Zn anode is limited by critical issues of dendrite growth and spontaneous side-reactions, which cause degradation of battery performance and potential safety issues. [2a,5]

Recent researches have been focused on extending the service life of AZBs by improving the stability of the Zn anode. Extensive efforts have been made by substrate design, [6] electrolyte/gel electrolyte optimization, [7] anode surface modification, [8] and hierarchical structure/

morphology construction of Zn anode. [9] However, most of these approaches generally require addition of extra components (e.g., a protective layer over Zn anode), or constructing sophisticated structures, thus increasing the cost or lowering the energy density of the entire device. Recently, it has been found that separator of AZBs does play a significant role in controlling the plating/stripping behaviors of Zn anode and the entire performance of AZBs. The main function of the separator in a battery is to prevent the electrical contact between the electrodes while allowing the transport of ions, which is crucial to the safe operation and electrochemical performance of a battery.[10] Thus far, many studies focused on the separator of AZBs. For example, Li et al.[11] developed a Janus separator via directly growing vertical graphene platelets on commercial glass fibers (GF), and they found that such a separator in AZBs can effectively protect the Zn anode. Yufit et al. [12] revealed that a microporous separator could not prevent the formation of zinc dendrites, and dendrites can grow inside the separator and eventually penetrate the separator. Among these studies, materials selected for AZB separators include GF,[11] cellulose/filter membranes, [13] and polypropylene. [14] However, these conventional materials cannot fully satisfy the requirements of a high performance separator, including low thickness, high porosity, sufficient mechanical strength, high electrolyte wettability, and low cost.[10,15] Meanwhile, these materials can hardly induce the

www.advancedsciencenews.com

www.afm-journal.de

1616208, 2023, 5, Downloaded from https://advanced.onlinelibrary.wiley.com/doi/10.1002/affm.202209301 by University Town Of Shenzhen, Wiley Online Library on [20/11/2025]. See the Terms and Conditions (https://onlinelibrary.wiley.com/terms-and-conditions) on Wiley Online Library for rules of use; OA acriles are governed by the applicable Cerative Commons I

uniform distribution and deposition of Zn^{2+} , resulting in low Coulombic efficiencies, poor cyclability, and premature device failure. [13b]

Recently, we found that the number of solvation water of zinc ions heavily alters the deposition morphology, and the organic–inorganic composite protection layer can effectively shield anion and free H₂O to suppress side reactions.^[16] In addition, many recent researches on separators tend to neglect the possible effect of the separator on modulating the electrolyte structure, which has been proven to be critical to the anode performance. Therefore, instead of optimizing the anode itself, a high-performance separator may be an effective approach to solve the problem of Zn anodes in AZBs.

Herein, we demonstrate the production of meter-sized highperformance polyacrylonitrile/graphene oxide (PG) separators using our custom designed and built needle-less electrospinning system. Detailed analysis reveals that the PG separator exhibits many unique advantages: 1) PG separator can absorb a large volume of electrolyte through the hierarchical 3D zincophilic frameworks. 2) The solvation structure of Zn²⁺ can be altered by the coordination groups of -OH, -COOH, and -CN groups. 3) The low energy barrier for the migration of Zn-ions via hopping through the -CN functional groups allow the fast transport of Zn-ions along the PG nanofibers. Therefore, the PG separator is able to regulate the homogeneous planar deposition of zinc ions and suppress the vertical dendrite growth of Zn. As a result, the transference number of Zn²⁺ with a PG separator is as high as 0.74, and the ionic conductivity of Zn²⁺ is up to 7.69 mS cm⁻¹. Zn||Cu half-cells with PG separators exhibit excellent Coulombic efficiency of 99.82%. Zn||Zn symmetric cells with PG separators achieve inconceivable ultra-long cycle life over 1 year (maintaining a low polarization of 52 mV over 13 000 h at 1 mA cm⁻² for 1 mAh cm⁻²), and $Zn||Zn_{0.27}V_2O_5|$ full batteries with PG separators show superior cyclic stability after 2800 cycles with a capacity retention rate of 71.5%. This work demonstrates a new possibility to achieve stable Zn anode by mass-producible separators.

2. Results and Discussion

2.1. Production and Characterization of PG Separator

Electrospinning is an advanced nanofiber fabrication technology, which produces polymer nanofibers by overcoming the surface tension of Taylor cone droplets.^[17] Recent studies have found that electrospun nanofiber separators offer multiple advantages including abundant surface functional groups, [18] high porosity, [19] ultra-stretchability, [20] and high strength/toughness. [21] However, production of separators by electrospinning is a typically slow process, thus the use of electrospun separators in AZBs has been limited to lab-scale research. $^{[17]}$ Therefore, we developed a home-made needle-less electrospinning system to enable high-throughput production of nanofiber-based separators. The needle-less electrospinning system mainly consists of several needle-less spinning jets, a roll-to-roll platform, and a temperature-humidity control system (Figure S1, Supporting Information). The spinning solution is shaped into Taylor cones under a high voltage and sprayed parallel to the electric field to form nanofibers (**Figure 1**a). Considering the benefits of -CN functional groups of polyacrylonitrile $(\text{PAN})^{[22]}$ and the high mechanical strength as well as abundant hydrophilic functional groups of graphene oxide (GO), $^{[6,23]}$ we selected PAN/N, N'-dimethylformamide solution with GO additive (Figure S2, Supporting Information) to fabricate electrospun nanofiber films, which were directly used as separators in AZBs. Using our needle-less electrospinning system, we were able to produce a continuous 50 cm wide film $(69~\mu\text{m}$ thick) at a rate of 10 m h⁻¹ (Figure 1b), and this production rate is about 200 times faster than traditional single-needle electrospinning technique. $^{[17]}$

Separators based on cellulose fibers (CF) and GF were widely used in aqueous batteries (Figures S3 and S4, Supporting Information), and they were selected as references to be compared with the PG separator in this study. XPS spectra confirmed that PG separator contains C, N, and O elements (Figure S5a–d, Supporting Information), and SEM and TEM images showed that PG separator consisted of uniform nanofibers (Figure 1c,d), as the schematic diagram shown in Figure 1e. The functional groups of CF and GF separators were identified by Fourier transform infrared spectrometer (FTIR) (Figure S5e, Supporting Information). In addition, FTIR spectra show that GO contain —OH and —COOH functional groups, and PAN has—CN functional group (Figure S5f, Supporting Information). [22]

Mechanical strength and hydrophilicity are two critical properties dictating the performance of a separator. The mechanical strength of the separators was tested using a tensile test and the results are shown in Figure 1f. Apparently, the ultimate tensile strength of PG separator is significantly higher than those of CF and PG separators (7.1 MPa vs 0.7 and 1.1 MPa). The tensile strength of PG separator is also higher than values reported for filter membrane (4.0 MPa), [13b] para-polybenzimidazole membrane (4.6 MPa),[24] and PAN separator (3.5 MPa).[22] The superior mechanical strength of PG is beneficial to effectively resist being punctured by the zinc dendrites.[13a] The electrolyte uptakes of three types of separators were measured as 397%, 1165%, and 2267% for CF, GF, and PG, respectively (Figure 1g and Table S1, Supporting Information). The high electrolyte uptake of PG suggests an excellent hydrophilicity of this material. The hydrophilicity of the separators was further confirmed by contact angle measurement (Figure 1h). Both GF and PG separators displayed the same contact angle of 0°, while the contact angle of CF separator was 16.9°. The 0° contact angle of PG separator indicates its outstanding electrolyte affinity, which largely originates from its abundant hydrophilic functional groups, such as carboxyl and hydroxyl from GO, as verified in the FTIR analysis. In summary, PG separator was successfully produced in meter-size and demonstrated excellent mechanical strength, electrolyte uptake, and hydrophilicity. All these advantages over conventional CF and GF separators are crucial for being high-performance AZB separators.

2.2. Effect of PG Separator on Zn2+

For comprehensive reasons, we chose 0.5 wt% GO in PAN (PG-0.5) as the optimum ratio of PG separator, which is explained in Figure S6, Supporting Information. To evaluate the performance of PG separator, we carried out Zn

16163028, 2023, 5, Downloaded from https://adv

elibrary.wiley.com/doi/10.1002/adfm.202209301 by University Town Of Shenzhen, Wiley Online Library on [20/11/2025]. See the Terms

ind-conditions) on Wiley Online Library for rules of use; OA articles are governed by the applicable Creative Commons

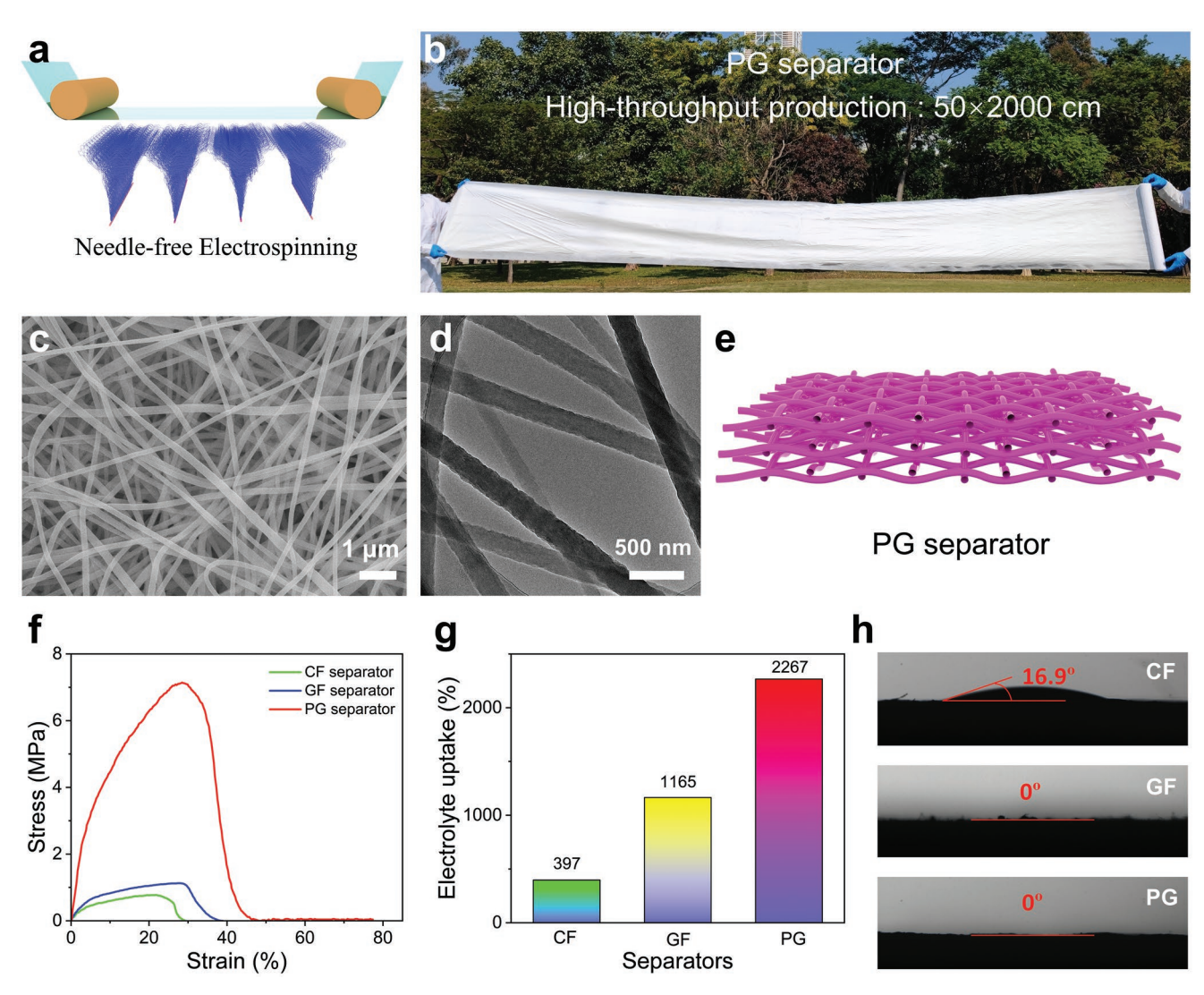


Figure 1. High-throughput production of PG separator. a) Schematic illustration of needle-less electrospinning process. b) High-throughput production of meter-sized PG separator. c) SEM and d) TEM images of PG separator. e) Schematic diagram of PG separator, f) tensile stress–strain curves, g) electrolyte uptake, and h) wettability with 3 M Zn(OTf)₂ electrolyte of CF, GF, and PG separators.

plating/stripping tests in Zn||Zn symmetric cells using 3 м Zn(OTf)₂ electrolyte with CF, GF, and PG separators (1 mA cm⁻² for 1 mAh cm⁻²). SEM images and the corresponding optical pictures of the three separators before and after 100 cycles are shown in Figure 2a-g. SEM images of the original CF, GF, and PG separators reveal that the average diameter of PG fibers is around 150 nm, much smaller than that of CF (≈22 µm) and GF (≈280 nm) fibers, and the thickness of PG separator is 69 µm, much thinner than that of CF (254 µm) and GF (337 nm) separators (Figure 2a-c and Figure S7, Supporting Information). Since the specific surface area is inversely proportional to the fiber size, the finer fibers in PG separator can offer more surface sites for adsorbing Zn²⁺. Obvious zinc deposits appeared on the surface of CF and GF separators after 100 cycles (Figure 2d,e and Figure S8a,b, Supporting Information). On the contrary, there was no visible zinc residues on the PG separator after the same number of plating/stripping cycles (Figure 2f and Figure S8c, Supporting Information), suggesting that the deposition of zinc is more uniform without generating macroscale deposits or debris. Usually the dendrite is more fragile than bulk zinc and tends to disintegrate. For verification, the zinc anodes from the three cells after 100 cycles were analyzed using SEM and confocal laser scanning microscope. As shown in Figure S9, Supporting Information, vertically aligned platelets were grown on the Zn anodes with CF and GF separators after 100 or 200 cycles, leading to very coarse surfaces. In contrast, the surface of the Zn anode with PG separator was much smoother, indicating that the plating of Zn was more uniform during cycling. Therefore, the PG separator is able to regulate the homogeneous planar deposition of zinc ions and suppress the vertical dendrite growth of Zn.

Since dendrite growth is a direct result of non-uniform Zn deposition, the PG separator appears to be able to greatly defer the growth of dendrites. XRD and XPS were used to identify phases and elements in the surface of Zn anodes after cycling. The Zn anode with the PG separator contained only

16163028, 2023, 5, Downloaded from https

brary.wiley.com/doi/10.1002/adfm.202209301 by University Town Of Shenzhen, Wiley Online Library on [20/11/2025]. See the Terms

und-conditions) on Wiley Online Library for rules of use; OA articles are governed by the applicable Creative Commons

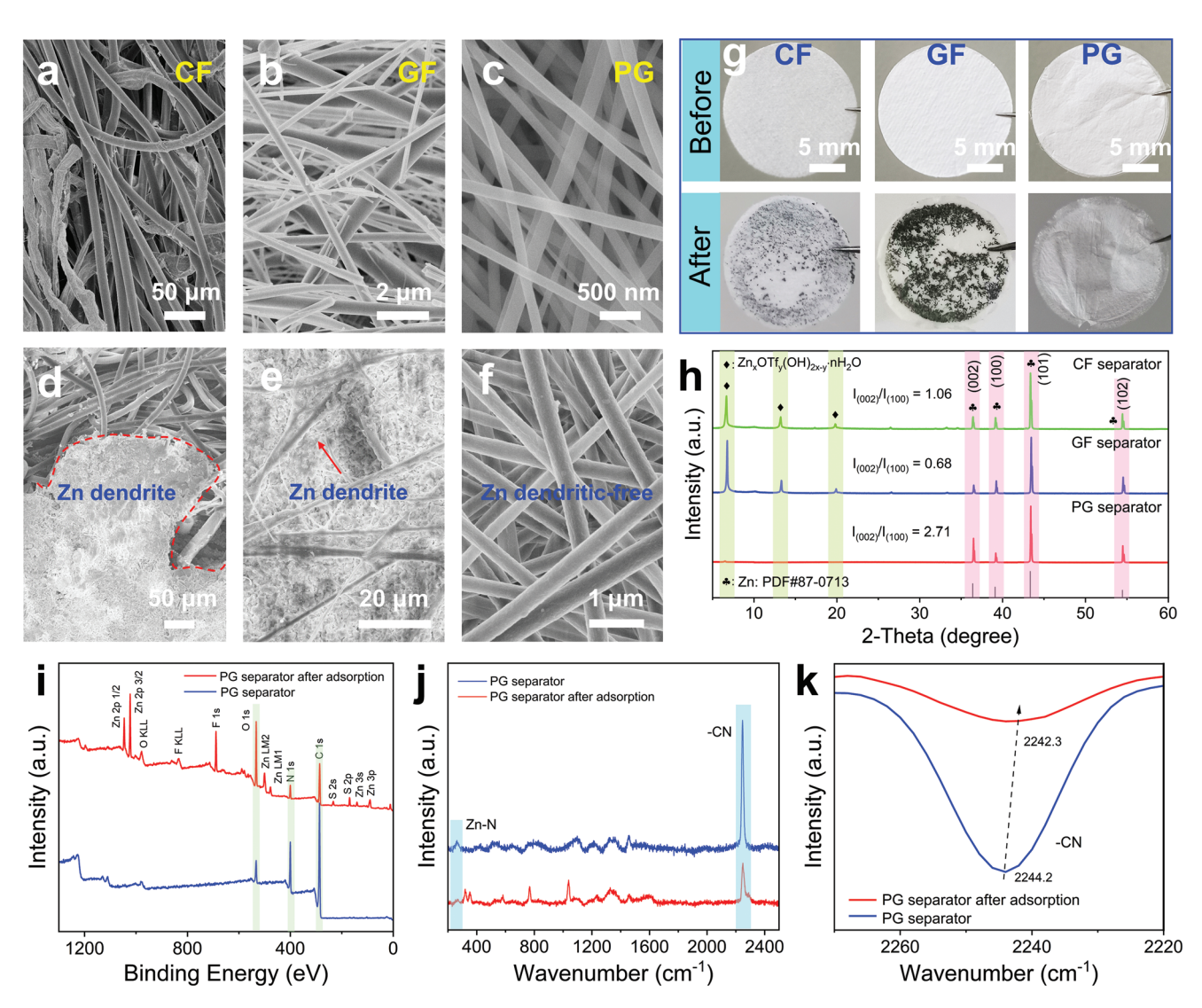


Figure 2. Characteristics of CF, GF, and PG separators before and after cycles/adsorption. a) CF, b) GF, and c) PG separators before cycle. d) CF, e) GF, and f) PG separators after cycles. g) Optical images of CF, GF, and PG separators before and after cycles. h) XRD patterns of Zn anodes with CF, GF, and PG separators after cycles. i) XPS, j) Raman, and k) FTIR spectra of PG separator before and after adsorption.

metallic zinc, while by-products from the salt species were found on the anodes with CF or GF separators (Figure 2h and Figure S10, Supporting Information).^[25] It appeared that the uniform plating of zinc also inhibited the undesirable side-reactions of the electrolyte, leading to more stable operation. The ratio between the intensities of the diffraction peaks of (002) to (101) planes of Zn anode after cycling with PG separator is 2.71, significantly higher than that of Zn anodes with CF (1.06) and GF (0.68) separators, suggesting a preferential orientation during the plating of Zn (Figure S11, Supporting Information). This may be due to the similar lattice parameter between the (002) plane of GO and (002) plane of Zn (only 7.4% linear mismatch).^[6,26] Consequently, the GO in the PG separator can effectively guide preferential growth of Zn along the (002) plane (Figure S12, Supporting Information).

We further investigated the underlying mechanism for the superior electrolyte affinity of PG separator. We first verified the adsorption of Zn²⁺ on the GO nanoplates using zeta-potential

measurement. The zeta-potential of GO alone in pure water was measured to be -42.8 mV (pH = 3.53). When GO was suspended in a 0.01 M ZnSO₄ solution, the zeta-potential was measured to be -8.8 mV (pH = 3.68) (Figure S13, Supporting Information). Apparently, positively charged Zn-ions are adsorbed on the negatively charged surface of GO under electrostatic attraction. The adsorption of zinc salt in the PG separator was analyzed using ex situ SEM, XPS, Raman, and FTIR. Before analysis, the PG separator was first soaked in 3 $\,\mathrm{M}$ Zn(OTf)₂ electrolyte for 2 h, and then washed and thoroughly dried. As shown in the EDS/SEM mapping, zinc salt from the electrolyte uniformly distributes inside the hierarchical 3D framework (Figure S14, Supporting Information). The XPS spectra of PG separator before and after salt soaking are shown in Figure 2i and Figure S15, Supporting Information. In particular, the N1s peak of PG separator after salt adsorption noticeably shifted by -1.38 eV compared to the pristine PG separator (Figure S15a, Supporting Information). The negative

16163028, 2023, 5, Downloaded from https://advanced.onlinelibrary.wiley.com/doi/10.1002/adfm.2022/9301 by University Town Of Shenzhen, Wiley Online Library on [20/11/2025]. See the Terms and Conditions (https://onlinelibrary.wiley.com/doi/10.1002/adfm.2022/9301 by University Town Of Shenzhen, Wiley Online Library on [20/11/2025]. See the Terms and Conditions (https://onlinelibrary.wiley.com/doi/10.1002/adfm.2022/9301 by University Town Of Shenzhen, Wiley Online Library on [20/11/2025]. See the Terms and Conditions (https://onlinelibrary.wiley.com/doi/10.1002/adfm.2022/9301 by University Town Of Shenzhen, Wiley Online Library on [20/11/2025]. See the Terms and Conditions (https://onlinelibrary.wiley.com/doi/10.1002/adfm.2022/9301 by University Town Of Shenzhen, Wiley Online Library on [20/11/2025]. See the Terms and Conditions (https://onlinelibrary.wiley.com/doi/10.1002/adfm.2022/9301 by University Town Of Shenzhen, Wiley Online Library on [20/11/2025].

ns) on Wiley Online Library for rules of use; OA articles are governed by the applicable Creative Commons

shift of the N 1s peak indicates the electron transfer between N and Zn, that is, the formation of Zn—N bonds.^[22,27] Meanwhile, the presence of the triflate ligands in the separator can be confirmed by the peak at 292.8 eV corresponding to —CF₃ in the C 1s spectra (Figures S5b and S15b, Supporting Information).^[28] In addition, the decrease in the intensity of Zn—N bond at 263 cm⁻¹ and the —CN characteristic peak at 2244 cm⁻¹ in Raman spectrum confirms the interaction between Zn²⁺ ions and —CN functional groups (Figure 2j).^[29] Furthermore, the wavenumber of —CN shifts from 2244.2 to 2242.3 cm⁻¹, suggesting the elongation of the —CN bond after Zn-ions were attached (Figure 2k and Figure S16, Supporting Information).^[30] Therefore, we conclude that the PG separator offers a hierarchical 3D zincophilic framework favoring electrolyte adsorption via both electrostatic and coordination interactions.

2.3. Electrochemical Performance of PG Separator

Generally, the function of PG separator can be explained by dehydration of solvated zinc ions, and regulation, the migration, and distribution of zinc ions in the separator, as shown in the schematic diagram of **Figure 3**a. This can be confirmed by the following electrochemical experiments. First, the Zn||Ti cells with PG separator displayed a lower nucleation overpotential (NOP) value of 56 mV than that of cells with CF (85 mV) and GF (77 mV) separators (Figure 3b), indicating that the PG separator could effectively decrease the local current density

and nucleation resistance during zinc deposition.[31] In addition, according to the cyclic voltammetry (CV) measurement results (Figure 3c), the cell with PG separator show higher current intensity and lower NOP than cells with CF and GF separators, most likely due to the faster kinetics of Zn²⁺ with a fewer number of coordinated water molecules migrating through the separator.^[32] Moreover, the transference number of Zn²⁺ was measured using chronoamperometry test. The transference number of Zn²⁺ with PG separator (0.74) is higher than with CF (0.35) and GF (0.26) separators, suggesting that the PG separator is favorable for Zn²⁺ migration (Figure 3d and Figure S17, Supporting Information).^[33] Furthermore, the ionic conductivity of the SS||SS (SS: stainless steel) cell with a PG separator was measured to be 7.69 mS cm⁻¹, which is higher than that of CF (1.55 mS cm⁻¹) and GF (1.89 mS cm⁻¹) separators, suggesting that PG separator can facilitate Zn²⁺ migration (Figure 3e,f).[33a] In summary, all above tests results reveal that PG separator can enhance the transport kinetics of Zn²⁺ ions compared with conventional separators (Table S18, Supporting Information).

2.4. Mechanistic Study of Zn²⁺ Migration through the PG Separator

To understand the transport kinetics of Zn²⁺ through the PG separator, we conducted first-principles calculations. Gaussian calculation was implemented to reveal the mechanism of PG

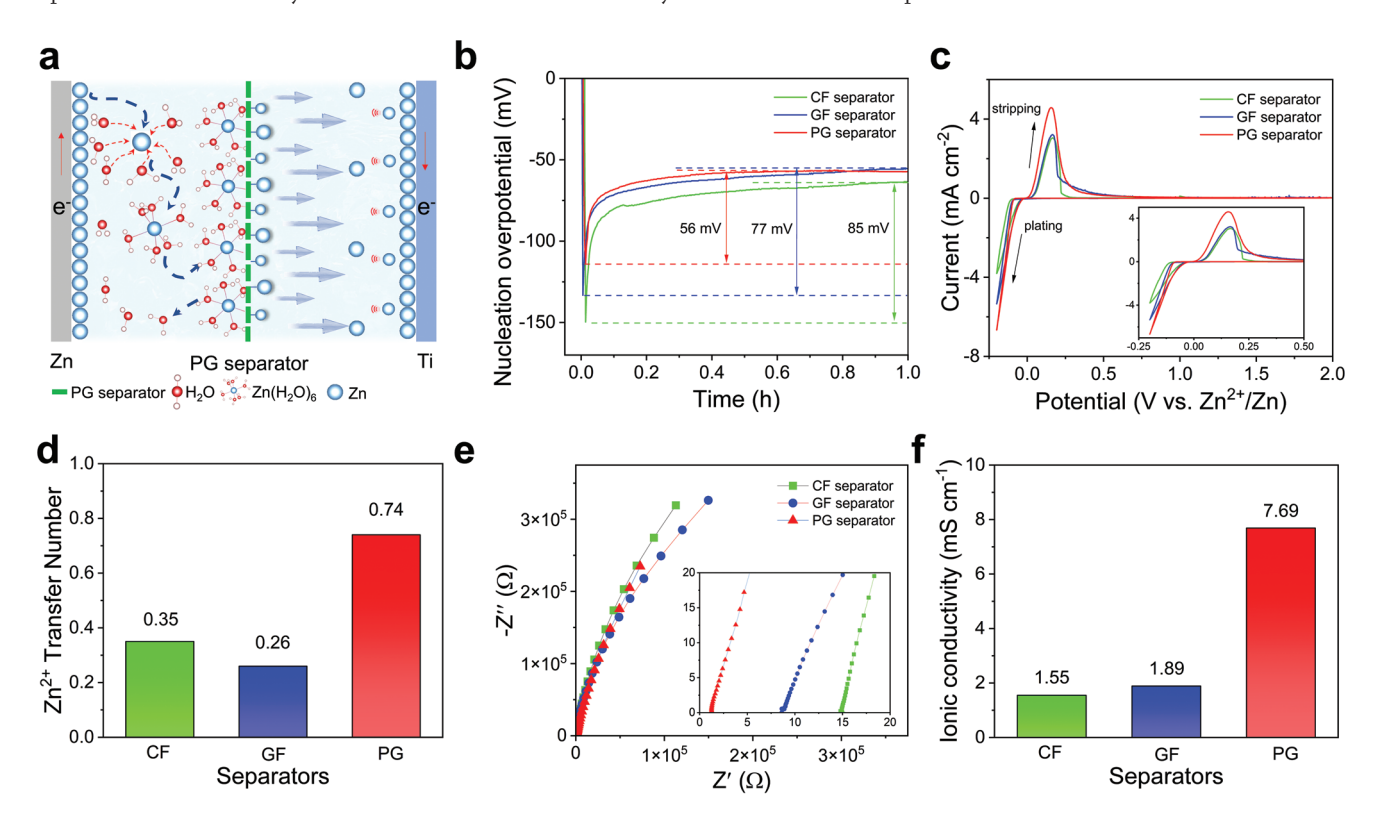


Figure 3. Electrochemical performance of CF, GF, and PG separators. a) Schematic diagram of Zn $\|$ Ti cells with PG separator. b) Nucleation overpotential-time profiles of Zn $\|$ Ti cells with CF, GF, and PG separators at scan rate of 0.5 mV s⁻¹. d) Zn²⁺ transfer number with CF, GF, and PG separators. e) Nyquist plots of SS $\|$ SS cells with CF, GF, and PG separators. f) Ionic conductivity of CF, GF, and PG separators.

16163028, 2023, 5, Downloaded from https:

edonlinelibrary.wiley.com/doi/10.1002/adfm.202209301 by University Town Of Shenzhen, Wiley Online Library on [20/11/2025]. See the Terms

ed by the applicable Creative Common

www.advancedsciencenews.com www.afm-journal.de

separator in modulating the coordination and transport of solvated Zn²⁺.^[16b,34] The -CN groups distribute regularly on the same side of the PAN chain in aqueous due to electrostatic interaction (Figures S18 and S19, Supporting Information). The

solvation energy of Zn^{2+} in water is -17.75 eV, which decreases to -20.59 and -20.30 eV after forming $[Zn(H_2O)_5(GO)_1]^{2+}$ and $[Zn(H_2O)_5(C_{3n}H_{3n}N_n)_1]^{2+}$ (n=7) respectively (**Figure 4a** and Figure S20, Supporting Information). The results suggest that

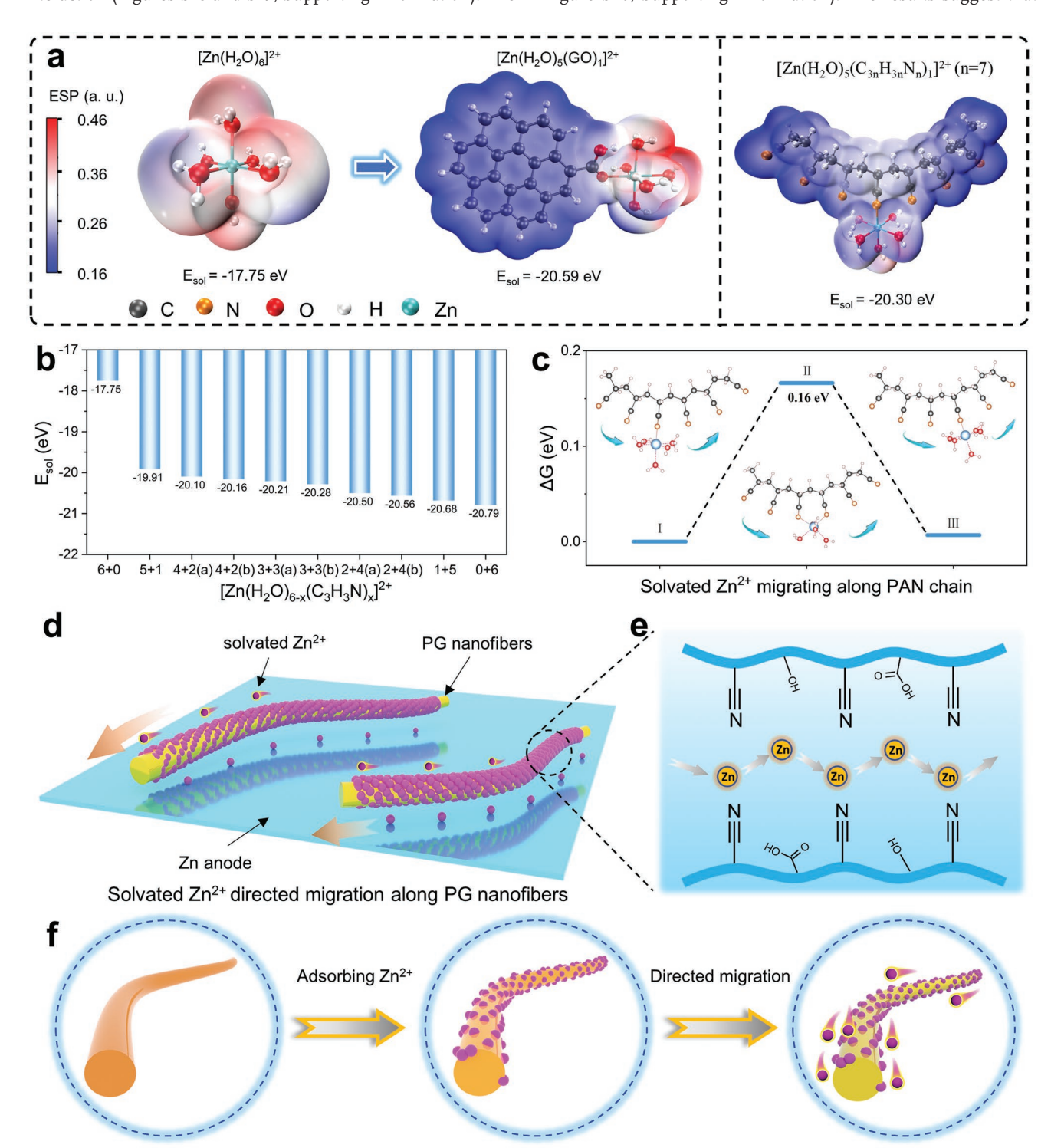


Figure 4. Directed migration mechanism of solvated Zn^{2+} transport along PG nanofibers, where solvated Zn^{2+} transport through -CN sites. a) Schematic diagram of electrostatic potential of $[Zn(H_2O)_6]^{2+}$, $[Zn(H_2O)_5(GO)_1]^{2+}$, and $[Zn(H_2O)_5(G_3,H_3,N_n)_1]^{2+}$ (n=7). b) The solvation energy of different coordination compositions of $[Zn(H_2O)_{6-x}(C_2H_3CN)_x]^{2+}$. c) The relative energy of solvated Zn^{2+} migrating along the PAN chain. d–f) Schematic diagram of solvated Zn^{2+} migrating along the directed migration paths of PG nanofibers targeting stabilized Zn anode.

1616/28/2, 2023, 5, Downloaded from https://advanced.onlinelibrary.wiley.com/doi/10.1002/affm.2020/2931 by University Town Of Sherzhen, Wiley Online Library on [20/11/2025]. See the Terms and Conditions (https://onlinelibrary.wiley.com/erms-and-conditions) on Wiley Online Library for rules of use; OA articles are governed by the applicable Creative Commons

both GO and PAN $(C_{3n}H_{3n}N_n)$ (n=7) are more nucleophilic than H₂O, and they prefer to coordinate with electrophilic Zn²⁺.^[35] In addition, a series of complexes $[Zn(H_2O)_{6-x}(C_2H_3CN)_x]^{2+}$ were established to inspect the coordination environment of solvated Zn2+, and the most stable configurations were determined by structural optimization (Figures S21-S30 and Tables S2-S11, Supporting Information). The result suggests that the distance of Zn-N in these complexes is generally shorter than that of Zn-O, implying the stronger bonding of Zn²⁺ with cyano ligand (Figure S31, Supporting Information). Furthermore, the solvation energy decreases obviously from -17.75 to -19.91 eV after dehydrating the first H₂O ligand to form $[Zn(H_2O)_5(C_2H_3CN)_1]^{2+}$ and then descends gradually to -20.79 eV in the subsequent dehydration process until the last H₂O ligand is replaced by C₃H₃N to form the most stable complex $[Zn(C_2H_3CN)_6]^{2+}$ (Figure 4b). This result demonstrates the huge thermodynamic driving force for capturing the solvated Zn²⁺ ions on PAN.

In order to further investigate the coordination environment of solvated Zn^{2+} more comprehensively, the possible complexes of Zn^{2+} coordinated with H_2O molecules and PAN with different degrees of polymerization ($C_{3n}H_{3n}N_n$, n=1 to 7) were constructed (Figures S22 and S32–S37 and Tables S3 and S12–S17, Supporting Information). The calculation results show that $[Zn(H_2O)_6]^{2+}$ has the highest solvation energy of -17.75 eV, which decreases abruptly to around -20 eV after dehydrating one H_2O molecule to form $[Zn(H_2O)_5(C_{3n}H_{3n}N_n)]^{2+}$, while this solvation energy is minimally affected by adjacent cyano ligands on PAN (Figure S38, Supporting Information). The shorter Zn-N distance than Zn-O in all complexes further substantiates that the electrostatic interaction between Zn and PAN is more significant than the $Zn-H_2O$ interaction in the solvation sheath (Figure S39, Supporting Information).

The migration energy barrier of Zn²⁺ along the PAN chain was estimated by calculating the Gibbs free energy change of Zn²⁺ hopping between two adjacent cyano ligands (Figure 4c). The $[Zn(H_2O)_5(C_{3n}H_{3n}N_n)_1]^{2+}$ complex first dehydrates one H₂O molecule to break its coordination structure, and then moves forward by the electrostatic attraction of the adjacent -CN. Subsequently, an intermediates state is formed with Zn²⁺ ion coordinating with two -CN. Finally, Zn²⁺ ion continues to migrate to the target place until the initial configuration $[Zn(H_2O)_5(C_{3n}H_{3n}N_n)_1]^{2+}$ is restored. In this process, the energy difference between the intermediate and initial states is only 0.16 eV, implicating the facile migration of Zn²⁺ ions along the PAN chains. All the above results reveal that PAN chains can successfully capture the Zn²⁺ ions from the aqueous solution and provide fast lanes for their migration, which can serve to regularize the distribution and dispersal behavior of Zn²⁺ ions across the whole separator, as shown in the schematic diagram of Figure 4d,e.

The desolvation process of Zn^{2+} and the directed migration mechanism of solvated Zn^{2+} transport along PG nanofibers can also be confirmed by relevant experiments. First, the chemical shift of 1H peak of acrylonitrile in 3 $_{\rm M}$ ZnSO $_{\rm 4}$ solutions in nuclear magnetic resonance spectrum confirms the desolvation process of Zn $^{2+}$ ions (Figure S40, Supporting Information). $^{[36]}$ In addition, Zn $^{2+}$ ions directed migration along the paths

of PG nanofibers can also be demonstrated by the diffusion experiment of zinc salt solution droplets infiltrating the separators (Figure S41, Supporting Information). The detailed discussion is provided in Supporting Information. Overall, the mechanism of Zn²⁺ ion transport can be concluded as follows (Figure 4f). First, the solvated Zn-ions are absorbed on the surface of PG nanofibers due to the affinity of Zn²⁺ ions to the functional groups therein. Subsequently, the Zn²⁺ ions are rapidly transported along the directed migration paths of the fibers, reaching a state where the distribution of Zn is spread across the PG separator. Finally, the PG separator can take the role of a templated skeleton for uniform deposition of Zn, thereby regulating the deposition kinetics and suppressing the growth of zinc dendrites.

2.5. Zn Plating/Stripping Reversibility with PG Separator

To elucidate the influence of PG separator on the Zn plating/ stripping behaviors compared to CF and GF separator, Zn||Cu half-cells and Zn||Zn symmetric cells were assembled by the three kinds of separators employing 3 M Zn(OTf)2 electrolyte (Figure 5 and Figures S42–S46, Supporting Information). Figure 5a shows the voltage-capacity profile of Zn||Cu halfcells with PG separator (1 mA cm⁻² for 0.5 mAh cm⁻²). The voltage gap is only 116 mV, which is much lower than that of CF (320 mV) and GF (146 mV) separators (Figures S42a and S43a, Supporting Information). Meanwhile, the corresponding average Coulombic efficiency of cells with PG separator is 99.82% over 1200 cycles, which is much higher than that of cells with CF (97.26% over 230 cycles) and GF (64.54% over 60 cycles) separators (Figure 5b and Figures S42b and S43b, Supporting Information). Obviously, the voltage of Zn||Cu halfcells with CF and GF separators fluctuated continuously during cycling (Figures S42c and S43c, Supporting Information), On the contrary, the voltage of Zn||Cu half-cells with PG separator is very stable during 1200 cycles (Figure S44, Supporting Information). Furthermore, the corresponding surface morphology and elemental distribution of Cu electrodes with CF and GF separators are uneven, but the surface of Cu electrode with PG separator is homogeneous (Figure S45, Supporting Information). This result indicates that the PG separator is able to regulate the homogeneous planar deposition of zinc ions with high reversibility and suppress the vertical dendrite growth of Zn.

The voltage hysteresis of Zn||Zn symmetric cells with PG separator increased from 56 to 65 mV as the current increased from 0.5 to 4 mA cm⁻², far smaller than that of cells with CF (120–158 mV at 0.5–2 mA cm⁻²) and GF (77–109 mV at 0.5–4 mA cm⁻²) separators (Figure S46, Supporting Information), suggesting the superior rate capacity achieved by the PG separator. In addition, we conducted a long cycling test using Zn||Zn symmetric cells at a high current density of 15 mA cm⁻² and capacity of 5 mAh cm⁻². The cell with PG separator showed a narrow voltage hysteresis of 202 mV in the first cycle, and stably operated for 4200 h. In comparison, cells with CF and GF separators showed wider voltage hysteresis (953 mV for CF and 306 mV for GF) in the first cycle and failed within

www.advancedsciencenews.com

www.afm-journal.de

16163028, 2023, 5, Downloaded from https://adv

onlinelibrary.wiley.com/doi/10.1002/adfm.202209301 by University Town Of Shenzhen, Wiley Online Library on [20/11/2025]. See the Terms

ons) on Wiley Online Library for rules of use; OA articles are governed by the applicable Creative Commons

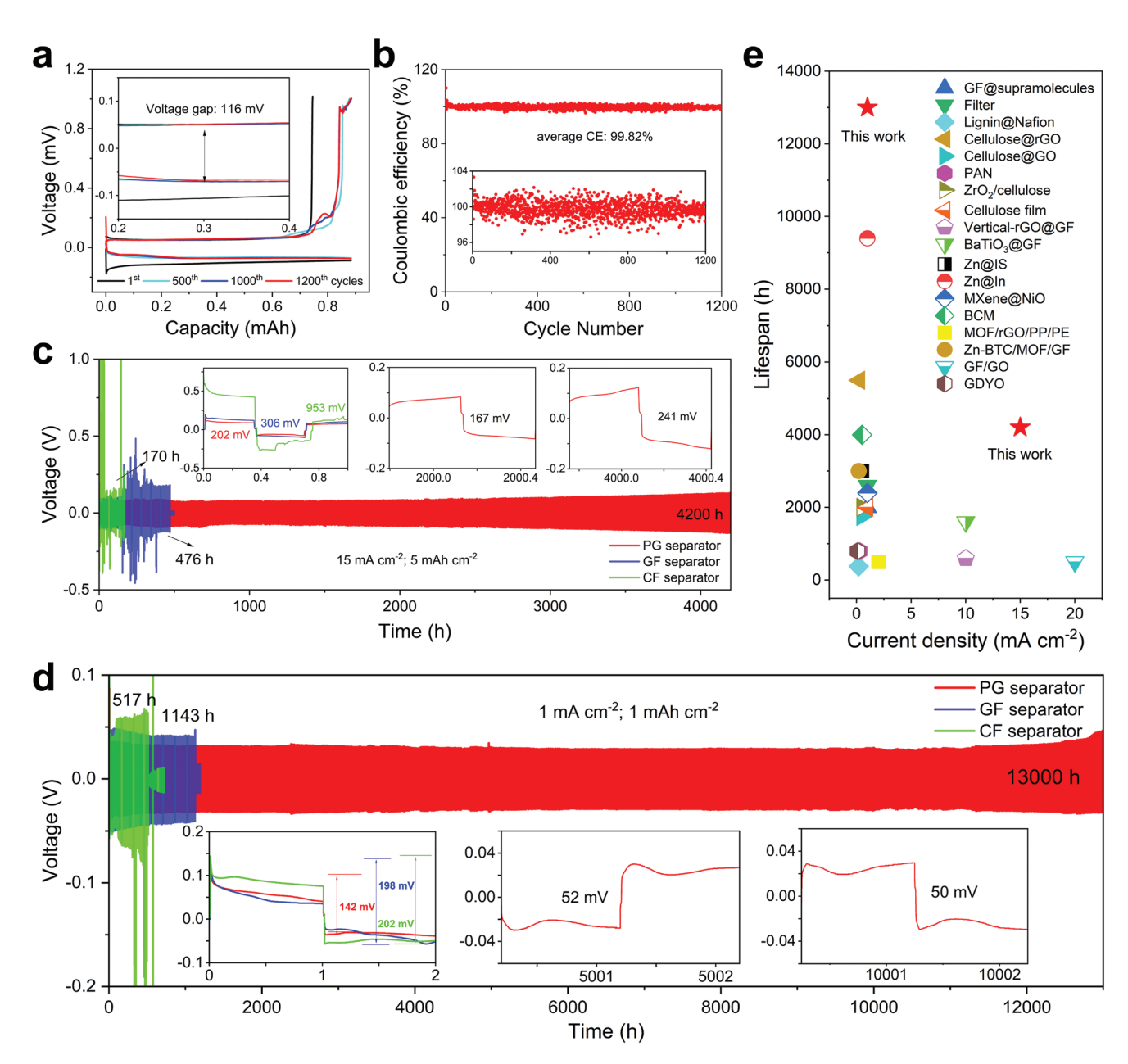


Figure 5. Electrochemical behaviors of $Zn\|Cu$ half-cells and $Zn\|Zn$ symmetric cells with CF, GF, and PG separators. a) Voltage—capacity profiles of the $Zn\|Cu$ half-cells with PG separator at 1 mA cm⁻² for 0.5 mAh cm⁻². b) Coulombic efficiency of $Zn\|Cu$ half-cells with CF, GF, and PG separators. Voltage—time profile of $Zn\|Zn$ symmetric cells with PG separator c) at 15 mA cm⁻² for 5 mAh cm⁻² and d) at 1 mA cm⁻² for 1 mAh cm⁻². e) Lifespan of $Zn\|Zn$ symmetric cells between our work and previous reported based on AZBs separators or surface modification.

500 h (170 h for CF and 476 h for GF) (Figure 5c). Furthermore, Zn||Zn symmetric cells with PG separators manifest ultra-long cycling life over 1 year (13 000 h, 1 mA cm $^{-2}$ for 1 mAh cm $^{-2}$) with a lower voltage hysteresis of 52 mV (Figure 5d). This result has exceeded most previous reports (Figure 5e and Table S19, Supporting Information). On the contrary, the symmetric cells with CF and GF separators experienced an abrupt voltage drop caused by short-circuiting after 517 and 1143 h, respectively (Figure 5d). These results demonstrate that the PG separator enhances the ability to stabilize the plating/stripping of Zn $^{2+}$ and prolong the cycling life of Zn anode.

2.6. Electrochemical Performance of AZBs Employing PG Separator

To evaluate the practical application of PG separator in AZBs, the electrochemical performance of $Zn||Zn_{0.27}V_2O_5$ full batteries with CF, GF, and PG separators were investigated (Figure 6). The $Zn_{0.27}V_2O_5$ cathode was synthesized according to the previous reference with slight modification.^[37] The stoichiometric ratio of $Zn_{0.27}V_2O_5$ was confirmed by ICPOES analysis (Table S20, Supporting Information), and the refined lattice parameters were derived from XRD spectrum

16163028, 2023, 5, Downloaded from https://adv

ntinelibrary.wiley.com/doi/10.1002/adfm.202209301 by University Town Of Shenzhen, Wiley Online Library on [20/11/2025]. See the Terms and Conditions (https://onlinelibr

on Wiley Online Library for rules of use; OA articles are governed by the applicable Creative Commons

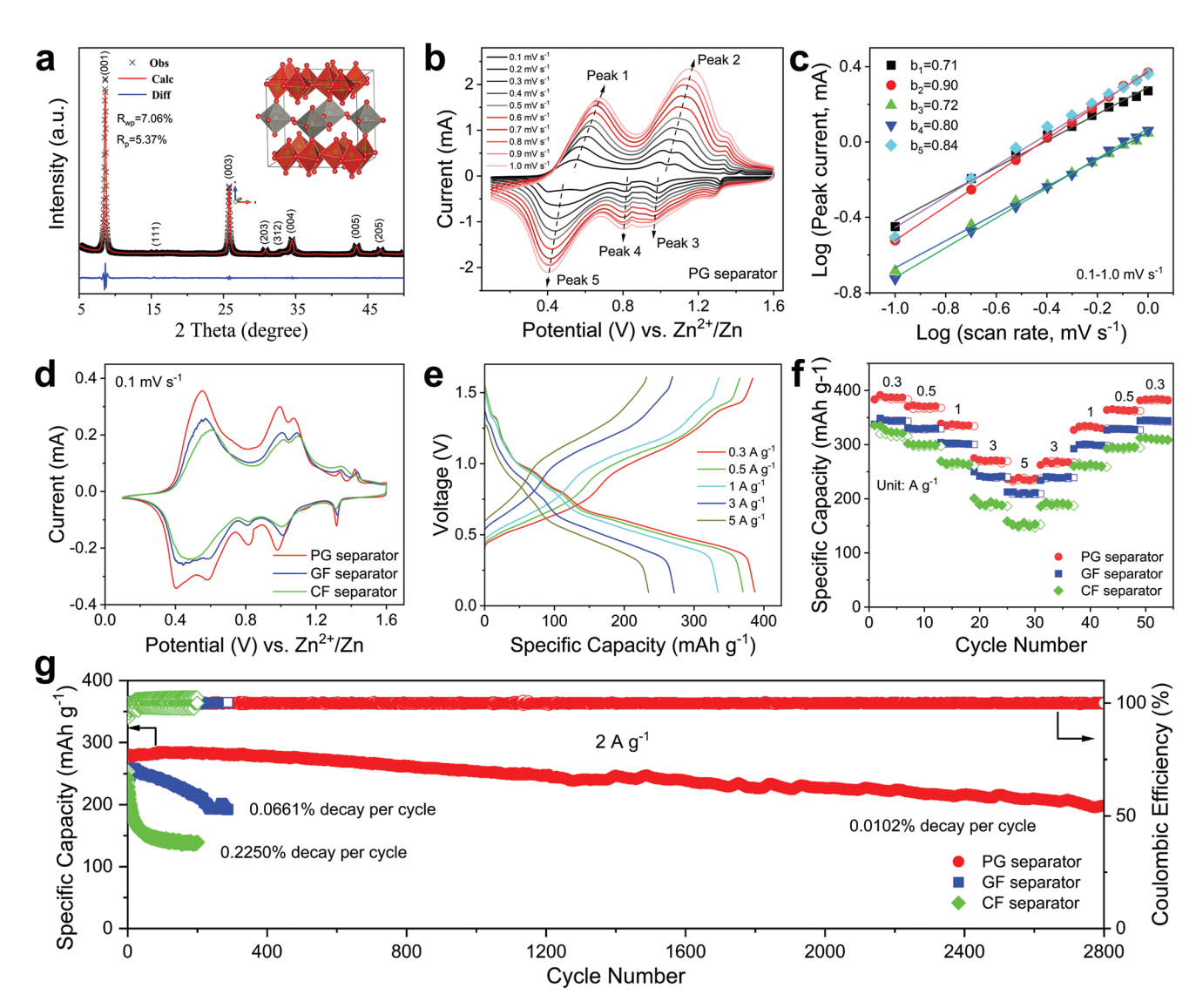


Figure 6. Electrochemical behaviors of $Zn\|Zn_{0.27}V_2O_5$ full batteries with CF, GF, and PG separators. a) Rietveld refinement data of $Zn_{0.27}V_2O_5$ cathode. b,c) CV curves of $Zn\|Zn_{0.27}V_2O_5$ batteries with PG separator at various scan rates, and log (i) versus log (ν) plots at specific peak currents, respectively. d) CV curves of $Zn\|Zn_{0.27}V_2O_5$ batteries with CF, GF, and PG separators at scan rate of 0.1 mV s⁻¹. e) Charge–discharge curves of $Zn\|Zn_{0.27}V_2O_5$ batteries with PG separator at various current densities. f) Rate capability plot of $Zn\|Zn_{0.27}V_2O_5$ batteries with CF, GF, and PG separators at various current densities. g) Cycle performances of $Zn\|Zn_{0.27}V_2O_5$ batteries at current density of 2 A g⁻¹.

(Figure 6a and Table S21, Supporting Information). The pristine $Zn_{0.27}V_2O_5 \cdot nH_2O$ were identified as nanobelts shape and contain 1.2 H_2O molecule (Figure S47, Supporting Information).

To further investigate the effect of separators on Zn^{2+} storage kinetics of $Zn_{0.27}V_2O_5$ electrodes, CV measurements were performed on $Zn\|Zn_{0.27}V_2O_5$ batteries with the three separators at different scan rates from 0.1 to 1.0 mV s⁻¹ (Figure 6b and Figure S48a,c Supporting Information). With the scan rate increasing, the shapes of CV curves with PG separator remain similar and the shift of redox peaks is subtle compared to CF and GF separators, indicating a fast and reversible Zn^{2+} intercalation/deintercalation even at the high scan rates. [38] Specifically, the two pairs of sharp redox peaks at 0.55/0.40 and 1.15/0.98 V are ascribed to the multi-step deintercalation/intercalation

of Zn^{2+} .^[39] And the small peaks appearing at 1.41/1.30 V are mainly caused by the chemical (de)intercalation and activation process of zinc ions in the $Zn_{0.27}V_2O_5$ materials.^[38] According to the relationship between applied current (*i*) and scan rate (v):^[40] $i = av^b$, where a and b are adjustable parameters, i and v are the applied current and scan rate. When the b value is close to 0.5, the electrochemical process is dominated by ionic diffusion, while the b value approached to 1.0, the surface-controlled response is leading. The calculated b values of peaks 1, 2, 3, 4, and 5 for the cells with PG separator are 0.71, 0.90, 0.72, 0.80, and 0.84, respectively, which are larger than those of the cells with CF and GF separators (Figure 6c and Figure S48b,d, Supporting Information), indicating that the PG separator facilitate the surface-controlled process. Meanwhile, the shapes of redox peaks are sharp, and the area enclosed by the CV curves

FUNCTIONAL

16163028, 2023. 5, Downloaded from https://advanced.onlinelibrary.wiley.com/doi/10.1002/adfm.202209301 by University Town Of Sherizhen, Wiley Online Library on [20/11/2025]. See the Terms and Conditions (https://onlinelibrary.wiley.com/ems/

and-conditions) on Wiley Online Library for rules of use; OA articles are governed by the applicable Creative Commons I

www.advancedsciencenews.com www.afm-journal.de

of $Zn\|Zn_{0.27}V_2O_5$ battery with PG separator is larger than that of CF and GF separators (Figure 6d). This indicates that PG separator not only supports faster charge transfer kinetics by facilitating Zn^{2+} platting/stripping evenly but also facilitates the capacity release.^[41]

In addition, electrochemical impedance spectrum was performed to further understand their electrochemical kinetics. The charge transfer resistance $R_{\rm ct}$ of PG separator (379.4 Ω) is lower than that of CF (1011.6 Ω) and GF (834.5 Ω) separators (Figure S49, Supporting Information), indicating PG separator apparently accelerate charge transfer during Zn²⁺ storage. [26] The rate performance of Zn||Zn_{0.27}V₂O₅ batteries with PG separator achieved high specific capacities of 386.7, 371.1, 336.0, 270.5, and 235.3 mAh g⁻¹ at current densities of 0.3, 0.5, 1, 3, and 5 A g⁻¹, respectively, which are superior to CF (321.3, 298.9, 264.5, 187.1, and 149.3 mAh g^{-1}) and GF (344.5, 328.2, 302.3, 238.7, and 210.4 mAh g⁻¹) separators atthe same current density (Figure 6e,f). Moreover, the cycling life of Zn||Zn_{0.27}V₂O₅ batteries with CF, GF, and PG separators were evaluated at a medium current density of 2 A g⁻¹, and the batteries with PG separator showed an impressive 71.5% retention rate over 2800 cycles (initial specific capacity of 277.8 mAh g⁻¹), accounting for merely 0.0102% decay per cycle and Coulombic efficiency maintenance of almost 100%. On the contrary, the full batteries with GF and CF separators underwent fast capacity decay, and the capacity decay per cycle is 0.0661% (81.0% retention rate over 288 cycles) for GF separator and 0.2250% (55.0% retention rate over 200 cycles) for CF separator, respectively (Figure 6g and Figure S50, Supporting Information). Meanwhile, the Zn||Zn_{0.27}V₂O₅ batteries with PG separators also showed a high capacity retention rate (74.5%) after 1000 cycles at a low current density of 0.5 A g⁻¹, which was superior to CF (28.1%) and GF (28.2%) separators (Figure S51, Supporting Information). Furthermore, the $Zn \| K_{0.36} H_{0.26} MnO_2$ batteries^[42] also demonstrated the compatibility of the PG separators with Mn-based cathode materials.^[43] The Zn||K_{0.36}H_{0.26}MnO₂ batteries showed an excellent rate performance and long-term cycling performance with 89.2% capacity retention over 900 cycles (Figure S52, Supporting Information).

To verify the performance of PG separator in near reallife products, Zn||Zn_{0.27}V₂O₅ pouch batteries were assembled and tested (Figure S53, Supporting Information). The Zn||Zn_{0.27}V₂O₅ pouch batteries with PG separator delivered high initial specific capacity of 252.6 mAh g⁻¹ and excellent capacity retention of 85.2% after 50 cycles at a current density of 2 A g⁻¹. After 50 cycles, we cut off about 20% of the pouch battery and the battery continued to work normally. Subsequently, we gradually cut off the pouch battery, eventually only 20% of the original battery volume was remained, and the battery continued to power an LCD alarm clock without any issue. The pouch battery was also flexible and could be wrapped around the wrist and still operated normally. In addition, we also fabricated two pouch batteries in series to light LEDs (Figure S54, Supporting Information). These encouraging results demonstrated the excellent safety and stability of the AZBs, and our work advanced the development of practical AZBs one more step forward.

3. Conclusions

In summary, we demonstrate that the PG separator has a dual function, providing a hierarchical 3D zincophilic framework favorable for electrolyte adsorption via electrostatic and chemical bonding interactions, as well as facilitating fiber-directed Zn²⁺ migration to form planar plating/stripping of Zn and suppressing dendrite growth. As a result, PG separator presents high ionic conductivity (7.69 mS cm⁻¹) and transference number of Zn²⁺ (0.74). More encouragingly, Zn||Zn symmetrical cells with PG separator achieve an enhanced CE (99.82%) and an inconceivable cyclic stability over 1 year (low polarization of 52 mV over 13 000 h at 1 mA cm⁻² for 1 mAh cm⁻²), and Zn||Zn_{0.27}V₂O₅ batteries with PG separator obtain a superior cyclic stability (0.0102% decay per cycle over 2800 cycles at 2 A g⁻¹). We anticipate that such directed transport pathway strategy of PG separator affording low cost and high performance would pave an innovative avenue for exploring next-generation high efficiency

Supporting Information

Supporting Information is available from the Wiley Online Library or from the author.

Acknowledgements

L.Y., C.H., and M.L. contributed equally to this work. This work was financially supported by Shenzhen Fundamental Research Program (No. GXWD20201231165207007-20200807111854001), the National Natural Science Foundation of China (52102201 and 22109003), and Soft Science Research Project of Guangdong Province (No. 2017B030301013). The authors are thankful for the support from the Test Center of the SAM-PKUSZ for Micro and Nanoscale Research and Fabrication, and the advanced computing resources from the Supercomputing Center of the SAM-PKUSZ.

Conflict of Interest

The authors declare no conflict of interest.

Data Availability Statement

The data that support the findings of this study are available from the corresponding author upon reasonable request.

Keywords

aqueous zinc-ion batteries, separators, zincophilicity functional groups, Zn anodes, Zn dendrite growths

Received: August 11, 2022 Revised: October 25, 2022 Published online: November 28, 2022

16163028,

, 2023, 5, Downloaded from https

onlinelibrary.wiley.com/doi/10.1002/adfm.202209301 by University Town Of Shenzhen, Wiley Online Library on [20/11/2025]. See the Terms

conditions) on Wiley Online Library for rules of use; OA articles are governed by the applicable Creative Cor

- [1] T. Liu, J. Liu, L. Li, L. Yu, J. Diao, T. Zhou, S. Li, A. Dai, W. Zhao, S. Xu, Y. Ren, L. Wang, T. Wu, R. Qi, Y. Xiao, J. Zheng, W. Cha, R. Harder, I. Robinson, J. Wen, J. Lu, F. Pan, K. Amine, *Nature* 2022, 606, 305.
- [2] a) F. Wang, O. Borodin, T. Gao, X. Fan, W. Sun, F. Han, A. Faraone,
 J. A. Dura, K. Xu, C. Wang, Nat. Mater. 2018, 17, 543; b) X. Jia,
 C. Liu, Z. G. Neale, J. Yang, G. Cao, Chem. Rev. 2020, 120, 7795.
- [3] M. Song, H. Tan, D. Chao, H. J. Fan, Adv. Funct. Mater. 2018, 28, 1802564.
- [4] a) Z. Yi, G. Chen, F. Hou, L. Wang, J. Liang, Adv. Energy Mater. 2021, 11, 2003065; b) X. Li, Z. Chen, Y. Yang, S. Liang, B. Lu, J. Zhou, Inorg. Chem. Front. 2022, 9, 3986.
- [5] J. Shin, J. Lee, Y. Park, J. W. Choi, Chem. Sci. 2020, 11, 2028.
- [6] J. Zheng, Q. Zhao, T. Tang, J. Yin, D. Q. Calvin, D. R. Genesis, X. Liu, Y. Deng, L. Wang, C. B. David, C. Jaye, D. Zhang, S. T. Esther, J. T. Kenneth, C. M. Amy, A. A. Lynden, *Science* 2019, 366, 645
- [7] a) L. Cao, D. Li, T. Pollard, T. Deng, B. Zhang, C. Yang, L. Chen, J. Vatamanu, E. Hu, M. J. Hourwitz, L. Ma, M. Ding, Q. Li, S. Hou, K. Gaskell, J. T. Fourkas, X.-Q. Yang, K. Xu, O. Borodin, C. Wang, Nat. Nanotechnol. 2021, 16, 902; b) C. Zhong, B. Liu, J. Ding, X. Liu, Y. Zhong, Y. Li, C. Sun, X. Han, Y. Deng, N. Zhao, W. Hu, Nat. Energy 2020, 5, 440; c) B. Zhang, L. Qin, Y. Fang, Y. Chai, X. Xie, B. Lu, S. Liang, J. Zhou, Sci. Bull. 2022, 67, 955.
- [8] a) Y. Zhang, M. Zhu, G. Wang, F.-H. Du, F. Yu, K. Wu, M. Wu, S.-X. Dou, H.-K. Liu, C. Wu, Small Methods 2021, 5, 2100650;
 b) L. Ma, Q. Li, Y. Ying, F. Ma, S. Chen, Y. Li, H. Huang, C. Zhi, Adv. Mater. 2021, 33, 2007406.
- [9] a) Q. Li, Y. Wang, F. Mo, D. Wang, G. Liang, Y. Zhao, Q. Yang, Z. Huang, C. Zhi, Adv. Energy Mater. 2021, 11, 2003931; b) P. Xue, C. Guo, L. Li, H. Li, D. Luo, L. Tan, Z. Chen, Adv. Mater. 2022, 34, 2110047
- [10] Y. Zhang, G. Yang, M. L. Lehmann, C. Wu, L. Zhao, T. Saito, Y. Liang, J. Nanda, Y. Yao, Nano Lett. 2021, 21, 10446.
- [11] C. Li, Z. Sun, T. Yang, L. Yu, N. Wei, Z. Tian, J. Cai, J. Lv, Y. Shao, M. H. Rümmeli, J. Sun, Z. Liu, Adv. Mater. 2020, 32, 2003425.
- [12] V. Yufit, F. Tariq, D. S. Eastwood, M. Biton, B. Wu, P. D. Lee, N. P. Brandon, *Joule* **2019**, *3*, 485.
- [13] a) W. Zhou, M. Chen, Q. Tian, J. Chen, X. Xu, C.-P. Wong, Energy Storage Mater. 2022, 44, 57; b) Y. Qin, P. Liu, Q. Zhang, Q. Wang, D. Sun, Y. Tang, Y. Ren, H. Wang, Small 2020, 16, 2003106.
- [14] D. J. Arnot, M. B. Lim, N. S. Bell, N. B. Schorr, R. C. Hill, A. Meyer, Y.-T. Cheng, T. N. Lambert, Adv. Energy Mater. 2021, 11, 2101594.
- [15] Q. Li, B. Yan, D. Wang, Q. Yang, Z. Huang, J. Fan, M. Dai, W. Chen, C. Zhi, Small 2022, 18, 2201045.
- [16] a) Y. Cui, Q. Zhao, X. Wu, X. Chen, J. Yang, Y. Wang, R. Qin, S. Ding, Y. Song, J. Wu, K. Yang, Z. Wang, Z. Mei, Z. Song, H. Wu, Z. Jiang, G. Qian, L. Yang, F. Pan, Angew. Chem., Int. Ed. 2020, 59, 16594;
 b) R. Qin, Y. Wang, M. Zhang, Y. Wang, S. Ding, A. Song, H. Yi, L. Yang, Y. Song, Y. Cui, J. Liu, Z. Wang, S. Li, Q. Zhao, F. Pan, Nano Energy 2021, 80, 105478.
- [17] J. Xue, T. Wu, Y. Dai, Y. Xia, Chem. Rev. 2019, 119, 5298.
- [18] L. Yue, H. Zhao, Z. Wu, J. Liang, S. Lu, G. Chen, S. Gao, B. Zhong, X. Guo, X. Sun, J. Mater. Chem. A 2020, 8, 11493.
- [19] X. Li, W. Chen, Q. Qian, H. Huang, Y. Chen, Z. Wang, Q. Chen, J. Yang, J. Li, Y.-W. Mai, Adv. Energy Mater. 2021, 11, 2000845.

- [20] P. Grandgeorge, N. Krins, A. Hourlier-Fargette, C. Laberty-Robert, S. Neukirch, A. Antkowiak, *Science* 2018, 360, 296.
- [21] X. Liao, M. Dulle, J. M. de Souza e Silva, R. B. Wehrspohn, S. Agarwal, S. Förster, H. Hou, P. Smith, A. Greiner, *Science* 2019, 366, 1376.
- [22] Y. Fang, X. Xie, B. Zhang, Y. Chai, B. Lu, M. Liu, J. Zhou, S. Liang, Adv. Funct. Mater. 2021, 32, 2109671.
- [23] Y. Zhu, S. Murali, W. Cai, X. Li, J. W. Suk, J. R. Potts, R. S. Ruoff, Adv. Mater. 2010, 22, 3906.
- [24] Y. Lu, Y. Wen, F. Huang, T. Zhu, S. Sun, B. C. Benicewicz, K. Huang, Energy Storage Mater. 2020, 27, 418.
- [25] P. Oberholzer, E. Tervoort, A. Bouzid, A. Pasquarello, D. Kundu, ACS Appl. Mater. Interfaces 2019, 11, 674.
- [26] J. Cao, D. Zhang, C. Gu, X. Wang, S. Wang, X. Zhang, J. Qin, Z.-S. Wu, Adv. Energy Mater. 2021, 11, 2101299.
- [27] J. B. Wang, H. M. Zhong, Z. F. Li, W. Lu, Appl. Phys. Lett. 2006, 88, 101913.
- [28] F. Wan, L. Zhang, X. Wang, S. Bi, Z. Niu, J. Chen, Adv. Funct. Mater. 2018, 28, 1804975.
- [29] K. Jindal, M. Tomar, R. S. Katiyar, V. Gupta, J. Appl. Phys. 2016, 120, 135305.
- [30] H. Yan, C. Han, S. Li, J. Liu, J. Ren, S. Yang, B. Li, Chem. Eng. J. 2022, 442, 136081.
- [31] T. Liu, J. Hong, J. Wang, Y. Xu, Y. Wang, Energy Storage Mater. 2022, 45, 1074
- [32] a) M. Ghosh, V. Vijayakumar, S. Kurungot, Energy Technol. 2019, 7, 1900442; b) Q. Lu, C. Liu, Y. Du, X. Wang, L. Ding, A. Omar, D. Mikhailova, ACS Appl. Mater. Interfaces 2021, 13, 16869.
- [33] a) J. Cao, D. Zhang, C. Gu, X. Zhang, M. Okhawilai, S. Wang, J. Han, J. Qin, Y. Huang, *Nano Energy* 2021, 89, 106322; b) Y. Yoshida, T. Yamada, Y. Jing, T. Toyao, K.-i. Shimizu, M. Sadakiyo, J. Am. Chem. Soc. 2022, 144, 8669.
- [34] a) J. Mink, C. Németh, L. Hajba, M. Sandström, P. L. Goggin, J. Mol. Struct. 2003, 661–662, 141; b) W. Yang, X. Du, J. Zhao, Z. Chen, J. Li, J. Xie, Y. Zhang, Z. Cui, Q. Kong, Z. Zhao, C. Wang, Q. Zhang, G. Cui, Joule 2020, 4, 1557.
- [35] F. Li, X. Jiang, J. Zhao, S. Zhang, Nano Energy 2015, 16, 488.
- [36] N. Dubouis, A. Serva, E. Salager, M. Deschamps, M. Salanne, A. Grimaud, J. Phys. Chem. Lett. 2018, 9, 6683.
- [37] D. Kundu, B. D. Adams, V. Duffort, S. H. Vajargah, L. F. Nazar, *Nat. Energy* 2016, 1, 16119.
- [38] X. Zhu, Z. Cao, X.-L. Li, L. Pei, J. Jones, Y.-N. Zhou, P. Dong, L. Wang, M. Ye, J. Shen, Energy Storage Mater. 2022, 45, 568.
- [39] Y. Yang, Y. Tang, G. Fang, L. Shan, J. Guo, W. Zhang, C. Wang, L. Wang, J. Zhou, S. Liang, Energy Environ. Sci. 2018, 11, 3157.
- [40] Y. Dai, X. Liao, R. Yu, J. Li, J. Li, S. Tan, P. He, Q. An, Q. Wei, L. Chen, X. Hong, K. Zhao, Y. Ren, J. Wu, Y. Zhao, L. Mai, Adv. Mater. 2021, 33, 2100359.
- [41] a) S. Deng, Z. Tie, F. Yue, H. Cao, M. Yao, Z. Niu, Angew. Chem., Int. Ed. 2022, 61, e202115877; b) Z. Li, Y. Xu, L. Wu, Y. An, Y. Sun, T. Meng, H. Dou, Y. Xuan, X. Zhang, Nat. Commun. 2022, 13, 132.
- [42] S. Ding, L. Liu, R. Qin, X. Chen, A. Song, J. Li, S. Li, Q. Zhao, F. Pan, ACS Appl. Mater. Interfaces 2021, 13, 22466.
- [43] a) Z. Liu, L. Qin, B. Lu, X. Wu, S. Liang, J. Zhou, ChemSusChem 2022, 15, 202200348; b) Z. Liu, Y. Yang, S. Liang, B. Lu, J. Zhou, Small Struct. 2021, 2, 2100119.